Journal of
Materials Chemistry A

PAPER

View Article Online
View Journal | View Issue

Check for updates

Cite this: *J. Mater. Chem. A*, 2025, **13**, 24925

Hydrazine oxidation-assisted electrocatalytic water splitting with Prussian blue analog-derived V-doped CoFe-layered double hydroxide nanosheets†

Baghendra Singh, Toufik Ansari and Arindam Indra *

Received 27th March 2025
Accepted 19th June 2025

DOI: 10.1039/d5ta02480c

rsc.li/materials-a

Efficient and sustainable hydrogen production through electrocatalytic water splitting remains a critical challenge, hindered primarily by the sluggish oxygen evolution reaction (OER). In this regard, leveraging the hydrazine oxidation reaction (HzOR) as an anodic alternative significantly lowers the overall cell voltage, promoting energy-efficient hydrogen evolution. In this study, we report Prussian blue analog (PBA)-derived vanadium-doped cobalt-iron layered double hydroxide (V-CoFe-LDH) nanosheets as an efficient electrocatalyst for the HzOR in the alkaline medium. The PBA-derived V-CoFe-LDH offered a high surface area, large porosity, and coordination unsaturation, and produced 2D nanosheets. The introduction of mixed-valence V^{4+}/V^{5+}-species modulated the electronic structure and enhanced the active site density, offering facile access to the higher oxidation states of Co and Fe-ions to improve the catalytic performance. The V-CoFe-LDH exhibited superior HzOR activity, achieving a significant reduction in the potential requirement (0.70 V in 3-electrode and 0.42 V in 2-electrode systems) compared to the anodic OER. Moreover, the structural modification in PBA-derived V-CoFe-LDH led to an improved HzOR compared to the hydrothermally prepared V-CoFe-LDH-HT. The *operando* Raman studies elucidated the formation of the $^*NH_2$ intermediate on the V-CoFe-LDH surface, and further confirmed the breaking of the N–N bond during the HzOR.

Introduction

Electrochemical hydrogen production by water splitting requires a high operational voltage (>1.23 V), leading to significant consumption of electricity and associated costs, which hinder its feasibility for large-scale implementation.[1–4] Therefore, developing efficient, energy-saving, and low-cost catalysts for hydrogen production has gained considerable importance.[1] In water splitting, the anodic oxygen evolution reaction (OER) works as the bottleneck because of its sluggish kinetics and high energy demand.[5–8] To overcome this, anodic oxidation reactions (AORs) of inorganic and organic substrates have been explored to lower the overall voltage requirement, increase the efficiency of the cell, and improve the hydrogen production rate.[9–13]

Among different AORs, the anodic hydrazine oxidation reaction (HzOR) is particularly important as it can largely improve hydrogen production.[14–16] As the HzOR requires a very low theoretical oxidation potential of −0.33 V *vs.* RHE, the replacement of the OER (theoretical potential is 1.23 V *vs.* RHE) by the HzOR can significantly reduce the operating voltage and, consequently, the energy demand, making it a highly attractive alternative for practical applications (Fig. 1).[17,18] Different research groups have explored HzOR-assisted H_2 production and analyzed the techno economical aspects.[19–24] For example, Badreldin *et al.* showed the economic feasibility of the HzOR over other anodic oxidation reactions.[19] The H_2 production cost (0.30 USD per kg H_2) by hydrazine oxidation was found to be economically viable compared to other anodic reactions like urea, methanol, ethanol oxidation, and the OER.[20] However, the high cost of hydrazine still poses a challenge for the commercial use of the HzOR.[20–24]

In recent years, substantial research has been directed toward the design of advanced electrocatalysts for catalyzing both the cathodic and anodic reactions in HzOR-assisted hydrogen production systems.[15,16,25–32] In this context, numerous electrocatalysts based on noble metals have been reported for electrocatalytic HzOR activity. For example, the $RhRu_{0.5}$-alloy,[33] AuPt alloy,[34] Rh_2P,[35] and so on have been developed for efficient HzOR coupled with the hydrogen evolution reaction (HER). Furthermore, transition metal-based catalysts such as $Ni(OH)_2/Ni_2P$,[36] P, W-Co_3N,[37] NiCoP,[38] NiCo-MOF/Mxene,[39] NiS_2,[40] and Co/MoO_2 (ref. 41) demonstrated

---

Department of Chemistry, Indian Institute of Technology (BHU), Varanasi, UP-221005, India. E-mail: arindam.chy@iitbhu.ac.in

† Electronic supplementary information (ESI) available: Catalyst synthesis, characterization, and optimization of the catalytic reactions. See DOI: https://doi.org/10.1039/d5ta02480c

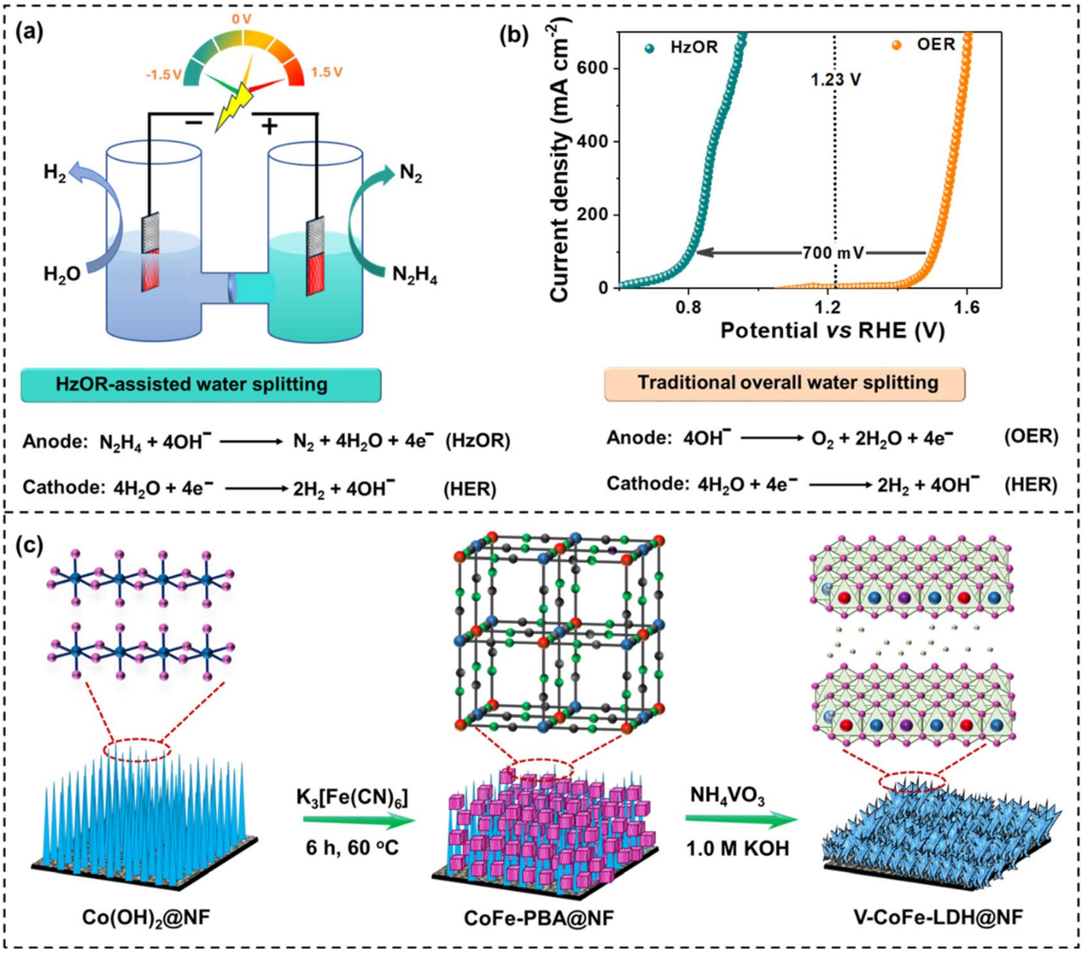

Fig. 1 (a) Schematic illustration showing hydrazine oxidation-assisted water splitting; (b) the advantages of hydrazine oxidation-assisted water splitting over traditional water splitting; and (c) alkaline etching of CoFe-PBA in the presence of NH_4VO_3 to produce V-CoFe-LDH. Color code of the atoms – Co: blue, O: pink, Fe: red, C: green, N: gray, V: purple.

excellent activity and stability for the HzOR.[42–45] In further advancement, researchers have extensively utilized transition metal-based hydroxides and layered double hydroxides (LDHs) for efficient HzOR.[36,46,47]

Interestingly, the use of a metal–organic framework (MOF) as the precursor of LDH was found to be beneficial for electrocatalytic performance.[48–51] MOF-derived LDHs provide a high surface area, atomic level thickness, tuned porosity, and optimized electronic properties for improved electrocatalytic activity and stability.[52–56] The electrocatalytic anodic oxidation activity of LDHs is further enhanced by the addition of high-valent metal ions.[56–58]

In this work, we have synthesized V-CoFe-LDH using CoFe-PBA as the precursor with simultaneous incorporation of V^{4+}/V^{5+}-ions during alkaline etching (Fig. 1). Previous work has demonstrated the synthesis of various hydroxides by the alkaline etching of PBAs.[59] Additionally, we have seen that PBAs undergo electrochemical conversion into M(O)(OH) nanosheets during the alkaline water splitting.[52–56] Nevertheless, it has not been investigated yet, how high-valent metal ions like V^{4+}/V^{5+} can be incorporated into PBA-derived LDH nanosheets to improve the electrocatalytic activity.

Previous studies indicate that the HzOR requires a highly efficient catalyst with excellent electronic conductivity and robust stability.[33–36,38,40] Moreover, the presence of high-valent metal ions significantly boosts the catalytic performance due to optimized electronic properties.[33–35,37,41,46,47] Herein, we combined multiple strategies to enhance the efficiency of the HzOR using V-doped CoFe-LDH catalysts: (i) the self-supported catalyst not only improves catalyst–support interactions but also facilitates charge transfer, improving the electrochemical activity and stability.[60] (ii) The introduction of V^{4+}/V^{5+}-ions in the structure of CoFe-LDH optimized the electronic structure, resulting in high catalytic efficiency.[61] (iii) The atomic-scale thin V-CoFe-LDH nanosheets offer coordination and electronic unsaturation at the metal centers with a high density of active binding sites for reactant molecules. (iv) The use of PBA as the precursor results in a large surface area, increased porosity, and modulated electronic properties in V-CoFe-LDH.[62]

As a result, V-CoFe-LDH nanosheets exhibited significantly improved HzOR activity compared to CoFe-LDH. Additionally, the incorporation of V^{4+}/V^{5+}-ions in CoFe-LDH was found to boost the efficacy of water splitting when the OER was substituted with the HzOR. The PBA-derived V-CoFe-LDH nanosheets achieved a current density of 100 mA cm^{-2} for the OER at the voltage demand of 1.50 V *vs.* RHE, while only 0.80 V *vs.* RHE was required for the HzOR. Additionally, V-CoFe-LDH manifested a cell potential of 1.22 V for 100 mA cm^{-2} current density for the HzOR, significantly lower than that of water splitting involving the anodic OER (1.64 V) in a two-electrode system. Furthermore, the efficiency of this newly developed catalyst was demonstrated by its remarkable HzOR activity compared to V-CoFe-LDH-HT, prepared by the hydrothermal method.

Results and discussion

Synthesis and characterization of the catalysts

Nickel foam-supported CoFe-PBA was synthesized following a methodology developed in our laboratory.[54,55] The formation of CoFe-PBA@NF was verified using powder X-ray diffraction (PXRD) and infrared (IR) spectroscopy and is outlined in the ESI (Fig. S1 and S2†). CoFe-PBA@NF was treated with ammonium metavanadate in an aqueous KOH solution, resulting in the formation of V-CoFe-LDH nanosheets (Fig. 1). Further, the amount of ammonium metavanadate was optimized by preparing two more vanadium-doped CoFe-layered double hydroxides (denoted as V-CoFe-LDH-1 and V-CoFe-LDH-2) to attain the highest HzOR activity. For comparison purposes, CoFe-LDH was also prepared by treating CoFe-PBA in an aqueous KOH solution without ammonium metavanadate. Additionally, a comparative V-CoFe-LDH-HT catalyst was synthesized by a hydrothermal method (Table S1†).

The V-incorporation in CoFe-LDH could happen in three possible ways; (i) introduction of V in the lattices of LDH replacing Co and Fe sites; (ii) intercalation of VO_x^{n-} between the layers of LDH; and/or (iii) both. To understand this process, we have carried out powder X-ray diffraction (PXRD). The PXRD pattern of both catalysts showed the characteristic peaks of CoFe-LDH (JCPDS no. 50-0235) (Fig. S3†). A positive shift of 0.12° in the two-theta angle of (003) and (015) peaks was observed for V-CoFe-LDH in contrast to CoFe-LDH. The incorporation of V^{4+}/V^{5+}, with smaller ionic radii than Co^{2+} and Fe^{3+}, into the lattice of CoFe-LDH led to lattice contraction and hence a positive shift in the PXRD peak of V-CoFe-LDH was observed.[50] This analysis confirmed the successful incorporation of V into the catalyst structure (Fig, S3†). On the other hand, intercalation of VO_x^{n-} between the layers of LDH has been ruled out as it leads to the expansion of the inter-planar distance.

Fourier transform infrared (FTIR) spectroscopy provided evidence for the formation of LDH. The FTIR spectrum of V-CoFe-LDH and CoFe-LDH revealed the absence of –CN bridges, characteristic of the PBA framework, indicating its decomposition and the formation of a new catalyst structure (Fig. S4†).[48,50] IR peaks of V-CoFe-LDH corresponding to the stretching and bending vibrations of the –OH group were observed at 3490 cm^{-1} and 1645 cm^{-1}, respectively. The FTIR spectrum of CoFe-LDH exhibited identical peaks with a positive shift of 6 cm^{-1} compared to V-CoFe-LDH (Fig. S4†). The combined PXRD and FTIR analyses validate the successful synthesis of V-CoFe-LDH.

Further, the electronic environment of the elements in the catalysts was examined by X-ray photoelectron spectroscopy (XPS). The major peaks in the Co 2p XPS of V-CoFe-LDH were observed at 782.08 eV and 797.74 eV for Co $2p_{3/2}$ and Co $2p_{1/2}$, respectively (Fig. 2a).[50,51,54] Deconvolution of Co $2p_{3/2}$ revealed the peaks for Co^{2+} and Co^{3+} at 784.26 eV and 781.91 eV, respectively. In comparison to CoFe-LDH, the Co $2p_{3/2}$ peak in V-CoFe-LDH was shifted by 0.57 eV toward higher binding energy. The Co^{3+}/Co^{2+} peak area ratio was higher for V-CoFe-LDH (1.66) in contrast to CoFe-LDH (0.47) (Fig. 2a).[50,51,54]

V-CoFe-LDH was found to have a Co $2p_{3/2}$-Co $2p_{1/2}$ spin–orbit coupling energy difference of 15.66 eV, indicating the presence of mixed-valent Co^{2+} and Co^{3+} species (Fig. 2a). The high Lewis acidic nature of V^{4+}/V^{5+} facilitated electron transfer from Co^{2+} to V^{4+}/V^{5+}, enhancing the electrophilicity of Co sites.[61]

In the Fe 2p XPS spectra of V-CoFe-LDH, peaks corresponding to Fe $2p_{3/2}$ and Fe $2p_{1/2}$ were observed at 710.84 eV and 723.57 eV, respectively (Fig. 2b).[50,51,54] Further fitting of the Fe $2p_{3/2}$ peak identified Fe^{2+} and Fe^{3+} species at 708.20 eV and 710.80 eV, respectively. Similar to Co 2p XPS, the Fe $2p_{3/2}$ peak of V-CoFe-LDH was shifted to a higher binding energy by 0.95 eV than CoFe-LDH, showing higher positive charge density on Fe in V-CoFe-LDH (Fig. 2b).[50,51,54] The Fe^{3+}/Fe^{2+} ratio in V-CoFe-LDH was found to be 1.94 while 1.30 was observed for CoFe-LDH.

Two peaks, representing V $2p_{3/2}$ and V $2p_{1/2}$ were deconvoluted from the V 2p XPS spectra of V-CoFe-LDH at 517.47 eV and 523.03 eV, respectively (Fig. 2c).[56,61] The signals at 517.50 eV and 519.29 eV validated the existence of V^{4+} and V^{5+} in V-CoFe-LDH. The binding energy of the V 2p spectrum of V-CoFe-LDH was observed between VO_2 and V_2O_5, further suggesting the presence of V^{4+} and V^{5+}.[63] The coexistence of V^{4+} and V^{5+} observed in the V 2p XPS can be attributed to the strong electronic interaction of vanadium with Co and Fe atoms. The strong Lewis acid V^{5+} ion withdraws electron density from Co and Fe-centers and gets reduced to V^{4+}.[56,61]

The O 1s XPS spectrum of V-CoFe-LDH displayed peaks at 529.62 eV, 532.35 eV, and 535.13 eV, corresponding to M–O bonds, surface –OH, and adsorbed H_2O, respectively (Fig. 2d).[56,61] The M–O peak in V-CoFe-LDH shifted negatively by 1.27 eV compared to CoFe-LDH, confirming electronic modifications due to V-doping (Fig. 2d).[56]

The morphological features of the catalysts were obtained from transmission electron microscopy (TEM) and scanning electron microscopy (SEM). SEM images showed that both V-CoFe-LDH and CoFe-LDH had a nanosheet morphology, with the nanosheets assembling into a flower-like structure (Fig. S5 and S6†). TEM studies further confirmed the nanosheet morphology of V-CoFe-LDH (Fig. 2e). High-resolution TEM (HRTEM) detected a lattice spacing of 0.23 nm, assigned to the (015) plane of CoFe-LDH (Fig. 2f).[64] Furthermore, the polycrystalline nature of V-CoFe-LDH was detected in the selected area electron diffraction (SAED) pattern (Fig. 2f inset). Atomic force microscopy analysis also showed 2–8 nm thickness of V-CoFe-LDH nanosheets (Fig. S7†).

Energy dispersive X-ray (EDX) spectroscopy confirmed the presence of Co, Fe, V, and O in V-CoFe-LDH and Co, Fe, and O in

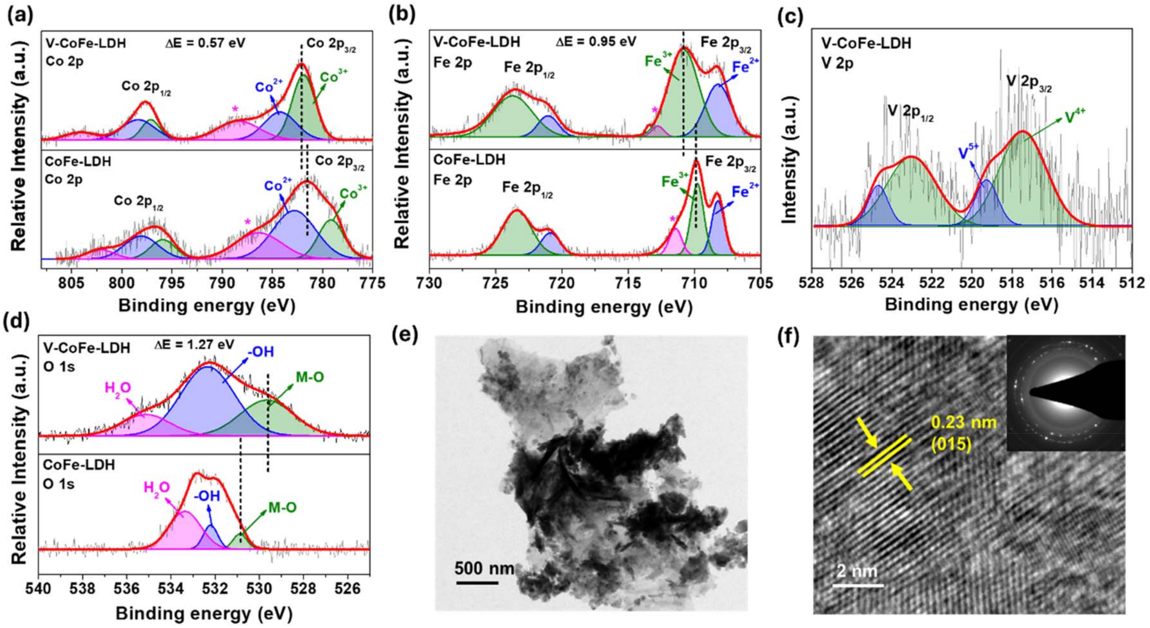

Fig. 2 (a) Co 2p XPS of CoFe-LDH and V-CoFe-LDH depicting a positive shift of the Co $2p_{3/2}$ binding energy in V-CoFe-LDH; (b) Fe 2p XPS of CoFe-LDH and V-CoFe-LDH showing a positive shift of the Fe $2p_{3/2}$ peak in V-CoFe-LDH; (c) V 2p XPS of V-CoFe-LDH showing the peaks for V^{4+} and V^{5+}; (d) O 1s XPS data of CoFe-LDH and V-CoFe-LDH showing the negative shift of the peak for the M–O bond in V-CoFe-LDH; (e) TEM image of V-CoFe-LDH; and (f) HRTEM image of V-CoFe-LDH showing the lattice spacing with a *d*-value of 0.23 nm for the (015) plane of LDH (SAED inset).

CoFe-LDH (Fig. S8 and S9†). EDX analysis also provided information about the elemental composition, specifically the Co and Fe ratios in V-CoFe-LDH and CoFe-LDH (Table S1†).

The EDX and XPS analyses showed a notable reduction in Fe content following vanadium incorporation in CoFe-LDH, suggesting the partial substitution of Fe by V in the catalyst structure. Further, XPS supports this observation by revealing shifts in the binding energies. More conclusive results were obtained from the PXRD studies (Fig. S3†). A positive shift in the two-theta value was observed for V-CoFe-LDH compared to CoFe-LDH. This shift can be explained by the lattice contraction, resulting from the substitution of Fe^{3+} ions in the LDH by V^{4+}/V^{5+} ions with smaller ionic radii. These results confirm the successful substitution of vanadium into the metallic sites of LDH.

Electrochemical characterization

The redox behavior of the metal sites in the catalysts was evaluated by cyclic voltammetry (CV). An oxidation peak at 1.31 V *vs.* RHE was visible in the CV of CoFe-LDH, corresponding to the Co^{2+}/Co^{3+} oxidation couple (Fig. 3a).[65]

V-CoFe-LDH manifested the Co^{2+}/Co^{3+} oxidation wave at a lower potential (1.29 V *vs.* RHE) than CoFe-LDH, suggesting that the inclusion of V facilitated the oxidation of Co^{2+} to Co^{3+}, enhancing O–O bond formation more effectively. In order to determine the quantity of active Co sites in the prepared catalysts, the redox peak area in the CV profile was integrated (Fig. S10†).[17,48] A larger number of active sites were observed in V-CoFe-LDH (14.24×10^{18} sites) compared to CoFe-LDH (3.71×10^{18} sites). The existence of a larger number of active sites in V-CoFe-LDH promoted facile binding of substrates and improved the catalytic activity.

Electrochemical impedance spectroscopy (EIS) showed the lower charge-transfer resistance (R_{ct}) of V-CoFe-LDH (0.59 Ω) than that of CoFe-LDH (1.90 Ω), indicating improved electron transfer due to V-introduction in the catalyst (Fig. 3b). The double-layer capacitance (C_{dl}) of V-CoFe-LDH was calculated to be 15.41 mF cm^{-2}, higher than that of CoFe-LDH (2.91 mF cm^{-2}) (Fig. 3c and S11†). Further, the electrochemical surface area (ECSA) values were calculated to be 385.25 cm^2 for V-CoFe-LDH and 72.75 cm^2 for CoFe-LDH (Fig. S11†).

Electrocatalytic water oxidation

The electrocatalytic OER performance of the catalysts was evaluated in 1.0 M KOH solution. The linear sweep voltammetry (LSV) revealed that CoFe-LDH achieved a current density of 100 mA cm^{-2} for the OER at a potential of 1.55 V *vs.* RHE (Fig. 3d). The introduction of V in CoFe-LDH lowered the required potential for the OER, reducing it to 1.50 V *vs.* RHE to deliver the same current density. Further, Tafel plots were utilized to assess the reaction kinetics of the developed catalysts. The Tafel slopes for V-CoFe-LDH and CoFe-LDH during the OER were determined to be 63 mV dec^{-1} and 128 mV dec^{-1}, respectively (Fig. S12†). These results confirmed that both the required potential and reaction kinetics were improved significantly when vanadium was introduced into the structure of CoFe-LDH.[66] As discussed earlier, V-incorporation in CoFe-LDH also improved the charge transfer kinetics (Fig. 3b).

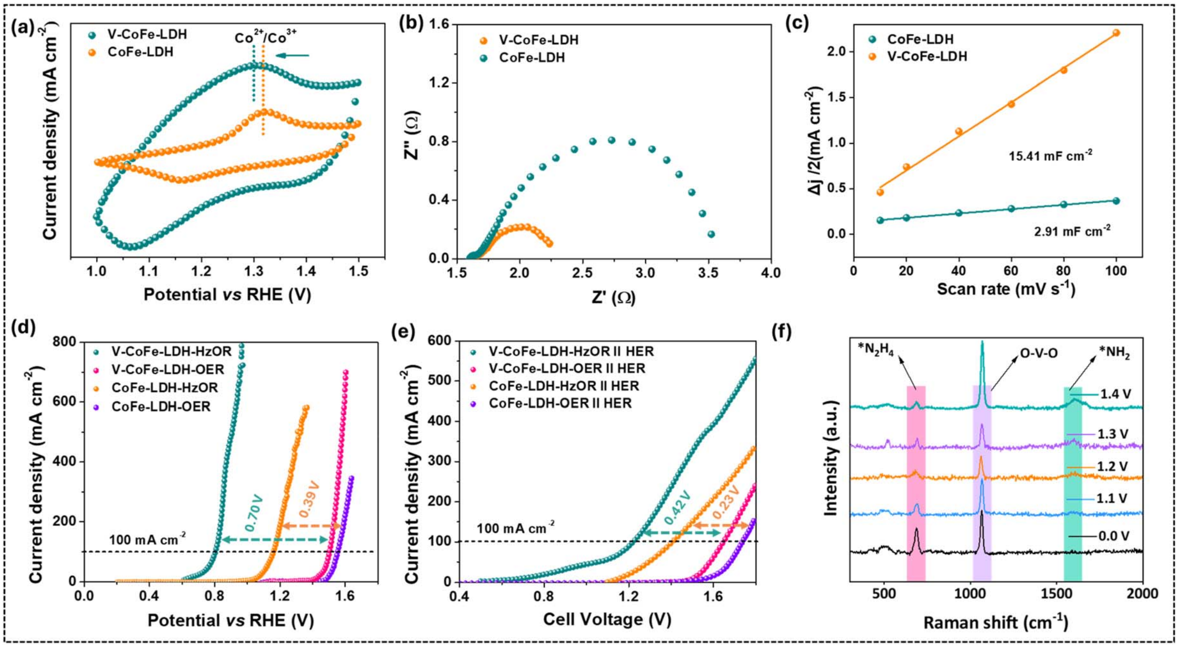

Fig. 3 (a) CV plots of CoFe-LDH and V-CoFe-LDH manifesting the oxidation peak of Co^{2+}/Co^{3+}; (b) EIS data of CoFe-LDH and V-CoFe-LDH showing the lower R_{ct} of V-CoFe-LDH; (c) C_{dl} profiles of CoFe-LDH and V-CoFe-LDH manifesting the larger C_{dl} of V-CoFe-LDH; (d) LSV profiles for the OER and HzOR activity of CoFe-LDH and V-CoFe-LDH verifying the excellent activity of V-CoFe-LDH; (e) LSV profiles for the overall water splitting activity of CoFe-LDH and V-CoFe-LDH in a two-electrode system with or without hydrazine; and (f) *operando* Raman spectroscopic studies of hydrazine oxidation at different cell voltages in a two-electrode set-up using V-CoFe-LDH as the anode and cathode (reaction conditions: 1.0 M KOH + 0.1 M N_2H_4, 25 °C).

Electrocatalytic hydrazine oxidation

The HzOR activity of the synthesized LDHs was demonstrated in 1.0 M KOH containing 0.1 M hydrazine. To achieve a high faradaic efficiency for the HzOR, it should be oxidized at a lower potential than the OER onset potential.[4] Interestingly, V-CoFe-LDH required 0.80 V *vs.* RHE to achieve 100 mA cm^{-2} current density when hydrazine (0.1 M) was added to the electrolyte (Fig. 3d). Even the HzOR takes place before the theoretical potential of water oxidation (1.23 V *vs.* RHE). This led to a marked reduction in the potential requirement (by 0.70 V) when the OER was substituted by the HzOR (Fig. 3d). The V-CoFe-LDH also avoided OER interference by achieving an industrial-level current density of 400 mA cm^{-2} at 0.87 V *vs.* RHE for the HzOR, which was below the onset potential for the OER (1.42 V *vs.* RHE) (Fig. 3d).

In contrast, the potential of CoFe-LDH for the HzOR was recorded to be 1.16 V *vs.* RHE with a reduction of 0.39 V compared to the OER with the same catalyst (Fig. 3d). Interestingly, V-CoFe-LDH manifested a significant potential reduction (0.70 V) for the HzOR in contrast to CoFe-LDH (0.39 V). This result established that the HzOR activity was significantly improved due to the incorporation of high valent V^{4+}/V^{5+} in CoFe-LDH. Further, the performance of V-CoFe-LDH surpassed that of V-CoFe-LDH-HT, V-CoFe-LDH-1, and V-CoFe-LDH-2 (Fig. S13†). The catalytic activity of V-CoFe-LDH for the HzOR was also found to be comparable to that of catalysts reported in the literature (Table S2†).

The OER and HzOR activities of V-CoFe-LDH were also evaluated in 0.1 M (pH: 12.12), 0.5 M (pH: 13.24), and 2.0 M (pH: 14.00) aqueous KOH solutions (Fig. S14 and S15†). The OER performances deteriorated in 0.1 M and 0.5 M KOH solutions while the activity was enhanced in 2.0 M KOH solution. Similarly, the HzOR performance declined in 0.1 M and 0.5 M KOH solutions, whereas in 2.0 M KOH, the activity remained nearly similar to that observed in 1.0 M KOH.

In further evaluation, V-CoFe-LDH was used as the anode and cathode to construct a two-electrode water electrolyzer. This electrolyzer manifested 100 mA cm^{-2} for overall water splitting at a cell voltage of 1.64 V (Fig. 3e). The cell voltage dropped to 1.22 V for the same current density when hydrazine was added to the electrolyte (Fig. 3e). This leads to a 0.42 V reduction in cell voltage for the HzOR compared to the OER. Moreover, V-CoFe-LDH also required a low cell voltage when compared with CoFe-LDH (Fig. 3e).

We have also carried out repeated chronoamperometric measurements for the HzOR for 5 cycles in a three-electrode system, demonstrating the excellent stability of V-CoFe-LDH for hydrazine oxidation (Fig. S16†). Furthermore, hydrogen production increased 3.9-fold during hydrazine oxidation relative to the OER (Fig. S17†).

In order to realize the reaction mechanism, the electrocatalytic hydrazine oxidation activity of V-CoFe-LDH was evaluated in a typical two-electrode system using an aqueous electrolyte containing 1.0 M KOH and 0.1 M N_2H_4 (Fig. 3f). After the introduction of N_2H_4 into the electrolyte, a strong Raman band appeared at 683 cm^{-1}, corresponding to the N–H stretching mode of adsorbed $^*NH_2NH_2$.[38] As the potential was applied, the intensity of the $^*NH_2NH_2$ peak decreased, while a new peak emerged at 1595 cm^{-1}, attributed to the $*NH_2$ intermediate.[38,67,68] Notably, the $*NH_2$ peak was not detectable at 0.0 V, but the intensity of the peak increased with increasing potential. This observation suggests that NH_2NH_2 is consumed during the reaction, leading to the formation of $*NH_2$ species. Based on these findings, the proposed reaction mechanism involves the initial adsorption of N_2H_4 on the V-CoFe-LDH surface to form $*NH_2NH_2$, followed by cleavage of the N–N bond to yield the $*NH_2$ intermediate. The $*NH_2$ species then undergoes stepwise dehydrogenation to produce N_2.[38,67]

The high HzOR activity of V-CoFe-LDH is attributed to strong Co 3d–O 2p–V 2p/Fe 2p orbital interactions and partial electron transfer from Co and Fe to V (Fig. S18†).[17,50] The Co^{3+} in its low-spin state ($t_{2g}^6e_g^0$) experiences significant electron–electron repulsion with the bridging O^{2-} ligand, while Fe^{3+} in its high-spin state ($t_{2g}^3e_g^2$) shows a poor electron–electron repulsion with the O^{2-} ligand.[17,50] The $3d^0$ outer electronic configuration of V^{5+}, characterized by empty t_{2g} and e_g orbitals, facilitates π-donation from the bridging oxygen atoms to the vanadium center.[17,50] This electron redistribution optimizes the electron density around the metal ions, stabilizing high-valent states and promoting catalytic activity.

The effect of V-doping on the electronic structure and catalytic activity of LDHs based on density functional theory (DFT) calculations were reported in the literature.[69–72] The DFT calculations revealed that the formation of O* from HO* is the rate-determining step on the NiFe-LDH surface.[70] After V-doping, the Gibbs free energy change of the rate determining step is reduced, facilitating the formation of O* to promote the O–O bond formation. Li *et al.* showed that the bandgap was significantly reduced after the doping of V in NiFe-LDH, improving the electronic conductivity.[70] Similarly, Jiang *et al.* explored V-doped nickel hydroxide for the OER and explained the improved activity by the DFT calculations.[71] The DFT calculations also revealed a higher water adsorption energy for V-$Co(OH)_2$ (1.14 eV) compared to $Co(OH)_2$ (0.60 eV).[73]

The crucial role of V in enhancing the catalytic HzOR activity of Ni_3N was also previously reported.[74] The V-doping in Ni_3N promotes the dehydrogenation of N_2H_4, thereby improving the efficiency of hydrazine oxidation. V-doping also modulates the reaction kinetics of the HzOR.[74] The DFT calculations revealed stepwise dehydrogenation of hydrazine involving intermediates $*N_2H_4$, $*N_2H_3$, $*N_2H_2$, $*N_2H$, and $*N_2$. Importantly, the dehydrogenation of N_2H_4 is the rate-determining step in the HzOR and it has a lower energy barrier on V-Ni_3N (0.27 eV) compared to Ni_3N (0.49 eV), indicating faster kinetics with the V-doped catalyst. Further, Bader charge analysis revealed weaker interaction between N_2H_3 and V-Ni_3N, consistent with the lower free energy barrier for this intermediate than that of Ni_3N. Overall, V-doping in the catalyst modulates the electronic structure, reduces the energy barrier and enhances HzOR activity.

Post-catalytic characterization

The anodic oxidation of an electrocatalyst leads to a change in the electronic as well as morphological features of the catalyst.[75,76] Therefore, post-catalytic characterization was conducted to detect the changes in the electronic as well as morphological features after anodic oxidation (120 h of HzOR CA).

A shift of 0.41 eV in the Co $2p_{3/2}$ peak towards higher binding energy was observed in the Co 2p XPS spectra of V-CoFe-LDH after CA, suggesting a higher concentration of Co^{3+} as a result of anodic oxidation (Fig. S19†).[50,51,54] The Co 2p XPS of CoFe-LDH after CA also manifested a positive shift of 0.16 eV in the Co $2p_{3/2}$ peaks in contrast to the fresh catalyst (Fig. S20†).[28,29,32] The Fe 2p XPS also showed a similar type of effect after anodic oxidation (Fig. S21 and S22†).[28,29,32] According to these findings, both catalysts produce high-valent metal ions during anodic oxidation. Likewise, upon CA, the V^{4+} and V^{5+} peaks in the V 2p XPS spectra of V-CoFe-LDH shifted negatively when compared with the fresh catalyst (Fig. S23†).[56]

The O 1s XPS analysis for V-CoFe-LDH after CA displayed three peaks with a positive shift of 0.88 eV in the M–O bond (Fig. S24†).[50,51,54] The O 1s XPS of CoFe-LDH also demonstrated a negative shift of 0.84 eV when compared with the fresh CoFe-LDH catalyst (Fig. S25†). The presence of V^{4+}/V^{5+} was confirmed from the V 2p XPS spectra, but with a decreased intensity, suggesting partial V leaching from the V-CoFe-LDH during anodic oxidation (Table S1†).[56]

The leaching of vanadium, as well as iron from the electrocatalysts during anodic oxidation, has also been previously reported by us and other groups.[56] Consequently, the surface analysis indicated a lower V content in the V-CoFe-LDH after CA in contrast to the fresh sample (Table S1†). In addition, we have performed ICP-AES analysis to understand the leaching of the metal ions during the catalytic process. A significant amount of V and Fe leaching was detected in the solution during the HzOR (Table S3†). However, the leaching of Fe in V-CoFe-LDH after CA was not as significant as previously reported in the case of the OER (Table S1†).[51,53,54]

The morphological features of V-CoFe-LDH after CA were investigated using SEM and TEM. SEM images showed the agglomeration of the nanosheets (Fig. S26†). The TEM images also confirmed the slight agglomeration after CA while HRTEM detected the (012) plane of CoFe-LDH with a lattice spacing of 0.25 nm (Fig. S27†).[76] Post-catalytic characterization verified that anodic oxidation produced more high-valent Co^{3+}/Fe^{3+}s-pecies with a slight variation in the catalyst's morphology.

Conclusions

In summary, we have developed high-valent V-doped CoFe-LDH nanosheets by the alkaline etching of a CoFe-PBA precursor. The incorporation of V^{4+}/V^{5+}-ions promotes electron withdrawal from Co and Fe sites. This electronic interaction speeds up reaction kinetics, enhances charge transfer, and raises the density of active sites. Consequently, V-CoFe-LDH achieved a current density of 100 mA cm^{-2} at 0.80 V *vs.* RHE for the HzOR, significantly lower than the 1.50 V required for the OER. It further reached an industrial-scale current density of 400 mA cm^{-2} at 0.87 V *vs.* RHE for the HzOR. In a two-electrode setup, substituting the OER with the HzOR reduced the cell voltage by 0.42 V, leading to a 3.9-fold increase in hydrogen production relative to the OER. The *operando* Raman analysis confirmed the cleavage of the N–N bond of hydrazine during the HzOR. This work thus presents a rational design approach for high-valent V-doped LDH nanosheets with enhanced HzOR activity.

Data availability

The data supporting this article have been included as part of the ESI.†

Author contributions

B. Singh: methodology, electrochemical measurement, characterization, data acquisition and formal analysis, writing the original draft; T. Ansari: electrochemical measurement, product analysis, Raman studies; A. Indra: project design, review and editing, supervision, conceptualization, resources and project administration.

Conflicts of interest

There are no conflicts of interest to declare.

Acknowledgements

A. I. acknowledges the core research grant (CRG/2023/002395). T. A. is grateful to PMRF, Govt. of India (ID: 1103080) for a fellowship.

References

1 Z. Li, L. Sun, Y. Zhang, Y. Han, W. Zhuang, L. Tian and W. Tan, *Coord. Chem. Rev.*, 2024, **510**, 215837.

2 Z. P. Ifkovits, J. M. Evans, M. C. Meier, K. M. Papadantonakis and N. S. Lewis, *Energy Environ. Sci.*, 2021, **14**, 4740–4759.

3 S. Anantharaj and S. Kundu, *ACS Energy Lett.*, 2019, **4**, 1260–1264.

4 J. Li and G. Zheng, *Adv. Sci.*, 2017, **4**, 1600380.

5 Y. Yan, B. Y. Xia, B. Zhao and X. Wang, *J. Mater. Chem. A*, 2016, **4**, 17587–17603.

6 K. Zhu, F. Shi, X. Zhu and W. Yang, *Nano Energy*, 2020, **73**, 104761.

7 F. Lyu, Q. Wang, S. M. Choi and Y. Yin, *Small*, 2019, **15**, 1804201.

8 Z. Kou, X. Li, L. Zhang, W. Zang, X. Gao and J. Wang, *Small Sci.*, 2021, **1**, 2100011.

9 D. Liu, Y. Cai, X. Wang, Y. Zhuo, X. Sui, H. Pan and Z. Wang, *Energy Environ. Sci.*, 2024, **17**, 6897–6942.

10 A. K. Singh, D. Kumar, B. Singh and A. Indra, *Synlett*, 2022, **34**, 552–560.

11 D. Yao, Y. Zhang, S. Zhang, J. Wan, H. Yu and H. Jin, *J. Mater. Chem. A*, 2023, **11**, 16433–16457.

12 C. Deng, C. Y. Toe, X. Li, J. Tan, H. Yang, Q. Hu and C. He, *Adv. Energy Mater.*, 2022, **12**, 2201047.

13 X. Liu, Y. Han, Y. Guo, X. Zhao, D. Pan, K. Li and Z. Wen, *Adv. Energy Sustainability Res.*, 2022, **3**, 2200005.

14 B. Singh and H. Gupta, *Chem. Commun.*, 2024, **60**, 8020–8038.

15 T. Y. Burshtein, Y. Yasman, L. Muñoz-Moene, J. H. Zagal and D. Eisenberg, *ACS Catal.*, 2024, **14**, 2264–2283.

16 K. Ojha, E. M. Farber, T. Y. Burshtein and D. Eisenberg, *Angew. Chem., Int. Ed.*, 2018, **57**, 17168–17172.

17 B. Singh, R. Kumar, T. Ansari, A. Indra and A. Draksharapu, *Chem. Commun.*, 2024, **60**, 9432–9435.

18 X. Xu, H. C. Chen, L. Li, M. Humayun, X. Zhang, H. Sun, D. P. Debecker, W. Zhang, L. Dai and C. Wang, *ACS Nano*, 2023, **17**, 10906–10917.

19 A. Badreldin, E. Youssef, A. Djire, A. Abdala and A. Wahab, *Cell Rep. Phys. Sci.*, 2023, **04**, 101427.

20 S. Lia, Y. Houa, L. Jiang, G. Fenga, Y. Gec and Z. Huang, *Energy Rev.*, 2025, **04**, 100105.

21 L. Zhu, J. Huang, G. Meng, T. Wu, C. Chen, H. Tian, Y. Chen, F. Kong, Z. Chang, X. Cui and J. Shi, *Nat. Commun.*, 2023, **25**, 1997.

22 S. Hu, H. Wu, C. Feng and Y. Ding, *Int. J. Hydrogen Energy*, 2020, **45**, 21040–21050.

23 A. Caravaca, A. de Lucas-Consuegra, A. B. Calcerrada, J. Lobato, J. L. Valverde and F. Dorado, *Appl. Catal., B*, 2013, **135**, 302–309.

24 C. R. Cloutier and D. P. Wilkinson, *Int. J. Hydrogen Energy*, 2010, **35**, 3967–3984.

25 Y. Liu, J. Zhang, Y. Li, Q. Qian, Z. Li and G. Zhang, *Adv. Funct. Mater.*, 2021, **31**, 2103673.

26 S. Singh, M. Yadav, D. K. Singh, D. K. Yadav, P. K. Sonkar and V. Ganesan, *New J. Chem.*, 2022, **46**, 13422–13430.

27 S. Zhang, C. Zhang, X. Zheng, G. Su, H. Wang and M. Huang, *Appl. Catal., B*, 2023, **324**, 122207.

28 J. Zhang, Y. Liu, J. Li, X. Jin, Y. Li, Q. Qian, Y. Wang, A. El-Harairy, Z. Li, Y. Zhu, H. Zhang, M. Cheng, S. Zeng and G. Zhang, *ACS Appl. Mater. Interfaces*, 2021, **13**, 3881–3890.

29 Q. Sun, L. Wang, Y. Shen, M. Zhou, Y. Ma, Z. Wang and C. Zhao, *ACS Sustain. Chem. Eng.*, 2018, **6**, 12746–12754.

30 X. Zhai, Q. Yu, G. Liu, J. Bi, Y. Zhang, J. Chi, J. Lai, B. Yang and L. Wang, *J. Mater. Chem. A*, 2021, **9**, 27424–27433.

31 Q. Sun, M. Zhou, Y. Shen, L. Wang, Y. Ma, Y. Li, X. Bo, Z. Wang and C. Zhao, *J. Catal.*, 2019, **373**, 180–189.

32 T. Shi, B. Gao, H. Meng, Y. Fu, D. Kong, P. Ren, H. Fu and Z. Feng, *Green Chem.*, 2024, **26**, 4209–4220.

33 X. Fu, D. Cheng, C. Wan, S. Kumari, H. Zhang, A. Zhang, H. Huyan, J. Zhou, H. Ren, S. Wang, Z. Zhao, X. Zhao, J. Chen, X. Pan, P. Sautet, Y. Huang and X. Duan, *Adv. Mater.*, 2023, **35**, 2301533.

34 Y. Yu, S. J. Lee, J. Theerthagiri, Y. Lee and M. Y. Choi, *Appl. Catal., B*, 2022, **316**, 121603.

35 Y. Zhao, N. Jia, X.-R. Wu, F.-M. Li, P. Chen, P.-J. Jin, S. Yin and Y. Chen, *Appl. Catal., B*, 2020, **270**, 118880.

36 H.-M. Yang, H.-Y. Wang, M.-L. Sun and Z.-Y. Yuan, *Chem. Eng. J.*, 2023, **475**, 146134.

37 Y. Liu, J. Zhang, Y. Li, Q. Qian, Z. Li, Y. Zhu and G. Zhang, *Nat. Commun.*, 2020, **11**, 1853.

38 L. Zhu, J. Huang, G. Meng, T. Wu, C. Chen, H. Tian, Y. Chen, F. Kong, Z. Chang, X. Cui and J. Shi, *Nat. Commun.*, 2023, **14**, 1997.

39 F. Sun, J. Qin, Z. Wang, M. Yu, X. Wu, X. Sun and J. Qiu, *Nat. Commun.*, 2021, **12**, 4182.
40 J. Wang, X. Ma, T. Liu, D. Liu, S. Hao, G. Du, R. Kong, A. M. Asiri and X. Sun, *Mater. Today Energy*, 2017, **3**, 9–14.
41 Y. Guo, X. Liu, Y. Zang, Y. Wu, Q. Zhang, Z. Wang, Y. Liu, Z. Zheng, H. Cheng, B. Huang, Y. Dai and P. Wang, *J. Mater. Chem. A*, 2022, **10**, 17297–17306.
42 G. Meng, Z. Chang, L. Zhu, C. Chen, Y. Chen, H. Tian, W. Luo, W. Sun, X. Cui and J. Shi, *Nanomicro Lett.*, 2023, **15**, 212.
43 M. Du, H. Sun, J. Li, X. Ye, F. Yue, J. Yang, Y. Liu and F. Guo, *Chemelectrochem*, 2019, **6**, 5581–5587.
44 B. Li, K. Wang, J. Ren and P. Qu, *New J. Chem.*, 2022, **46**, 7615–7625.
45 Y. Zhao, Y. Sun, H. Li, S. Zeng, R. Li, Q. Yao, H. Chen, Y. Zheng and K. Qu, *J. Colloid Interface Sci.*, 2023, **652**, 1848–1856.
46 G. Liu, Z. Wang, T. Shen, X. Zheng, Y. Zhao and Y.-F. Song, *Nanoscale*, 2021, **13**, 1869–1874.
47 Z. Li, M. Shao, H. An, Z. Wang, S. Xu, M. Wei, D. G. Evans and X. Duan, *Chem. Sci.*, 2015, **6**, 6624–6631.
48 B. Singh, T. Ansari and A. Indra, *ACS Appl. Nano Mater.*, 2024, **7**, 15754–15762.
49 B. Singh, A. Yadav and A. Indra, *J. Mater. Chem. A*, 2022, **10**, 3443–3468.
50 B. Singh, A. K. Patel and A. Indra, *Mater. Today Chem.*, 2022, **25**, 100930.
51 B. Singh, O. Prakash, P. Maiti, P. W. Menezes and A. Indra, *Chem. Commun.*, 2020, **56**, 15036–15039.
52 P. Mukherjee, K. Sathiyan, R. B. -Ziv and T. Zidki, *Inorg. Chem.*, 2023, **62**, 14484–14493.
53 T. Ansari, D. Bagchi, S. Ghosh, J. Niklas Hausmann, A. Indra and P. W. Menezes, *Chem.–Eur. J.*, 2025, **31**, e202404174.
54 B. Singh, P. Mannu, Y. C. Huang, R. Prakash, S. Shen, C. L. Dong and A. Indra, *Angew. Chem., Int. Ed.*, 2022, **61**, e202211585.
55 B. Singh, T. Ansari, N. Verma, Y.-C. Huang, P. M. Mannu, C.-L. Dong and A. Indra, *J. Mater. Chem. A*, 2024, **12**, 19321–19330.
56 B. Singh, Y.-C. Huang, A. Priyadarsini, P. Mannu, S. Dey, G. K. Lahiri, B. S. Mallik, C.-L. Dong and A. Indra, *J. Mater. Chem. A*, 2023, **11**, 15906–15914.
57 D. Zhou, P. Li, X. Lin, A. McKinley, Y. Kuang, W. Liu, W. F. Lin, X. Sun and X. Duan, *Chem. Soc. Rev.*, 2021, **50**, 8790–8817.
58 Z. Wang, W. Liu, Y. Hu, M. Guan, L. Xu, H. Li, J. Bao and H. Li, *Appl. Catal., B*, 2020, **272**, 118959.
59 W.-D. Zhang, X. Yan, T. Li, Y. Liu, Q.-T. Fu and Z.-G. Gu, *Chem. Commun.*, 2019, **55**, 5467–5470.
60 H. Yang, M. Driess and P. W. Menezes, *Adv. Energy Mater.*, 2021, **11**, 2102074.
61 B. Singh and A. Indra, *Dalton Trans.*, 2021, **50**, 2359–2363.
62 B. Singh, O. Prakash, P. Maiti and A. Indra, *ACS Appl. Nano Mater.*, 2020, **3**, 6693–6701.
63 J. Mendialdua, R. Casanova and Y. Barbaux, *J. Electron Spectrosc. Relat. Phenom.*, 1995, **71**, 249–261.
64 A. K. Singh, S. Ji, B. Singh, C. Das, H. Choi, P. W. Menezes and A. Indra, *Mater. Today Chem.*, 2022, **23**, 100668.
65 Y. Bi, Z. Cai, D. Zhou, Y. Tian, Q. Zhang, Q. Zhang, Y. Kuang, Y. Li, X. Sun and X. Duan, *J. Catal.*, 2018, **358**, 100–107.
66 Y. Fu, T. Li, G. Zhou, J. Guo, Y. Ao, Y. Hu, J. Shen, L. Liu and X. Wu, *Nano Lett.*, 2020, **20**, 4960–4967.
67 J. Lan, M. Luo, J. Han, M. Peng, Hu. Duan and Y. Tan, *Small*, 2021, **17**, 2102814.
68 K. Bera, A. Karmakar, S. Kumaravel, S. S. Sankar, R. Madhu, H. N. Dhandapani, S. Nagappan and S. Kundu, *Inorg. Chem.*, 2022, **61**, 4502–4512.
69 P. Li, X. Duan, Y. Kuang, Y. Li, G. Zhang, W. Liu and X. Sun, *Adv. Energy Mater.*, 2018, **8**, 1703341.
70 J. Liang, H. Shen, Y. Ma, D. Liu, M. Li, J. Kong, Y. Tang and S. Ding, *Dalton Trans.*, 2020, **49**, 11217–11225.
71 N. Wu and X. Du, *Int. J. Hydrogen Energy*, 2023, **48**, 23877–23884.
72 J. Jiang, F. Sun, S. Zhou, W. Hu, H. Zhang, J. Dong, Z. Jiang, J. Zhao, J. Li, W. Yan and M. Wang, *Nat. Commun.*, 2018, **9**, 2885.
73 J. Zhang, Y. Liu, J. Li, X. Jin, Y. Li, Q. Qian, Y. Wang, A. El-Harairy, Z. Li, Y. Zhu, H. Zhang, M. Cheng, S. Zeng and G. Zhang, *ACS Appl. Mater. Interfaces*, 2021, **13**, 3881–3890.
74 Y. Li, X. Du, J. Huang, C. Wu, Y. Sun, G. Zou, C. Yang and J. Xiong, *Small*, 2019, **15**, 1901980.
75 L. Gao, X. Cui, C. D. Sewell, J. Li and Z. Lin, *Chem. Soc. Rev.*, 2021, **50**, 8428–8469.
76 Z. Kong, J. Chen, X. Wang, X. Long, X. She, D. Li and D. Yang, *Mater. Adv.*, 2021, **2**, 7932–7938.